INTERNATIONAL JOURNAL FOR NUMERICAL METHODS IN FLUIDS
Int. J. Numer. Meth. Fluids 2000; **33**: 249–278

Evaluation of some high-order shock capturing schemes for direct numerical simulation of unsteady two-dimensional free flows

C. Tenaud[a,*], E. Garnier[b] and P. Sagaut[b]

[a] *Laboratoire d'Informatique pour la Mécanique les Sciences de l'Ingénieur (CNRS-UPR 3251), BP 133, F-91403 Orsay Cedex, France*
[b] *Office National d'Etudes et de Recherches Aérospatiales DSNA/ETRI BP 72, 29 Avenue de la Division Leclerc, F-92322 Châtillon Cedex, France*

SUMMARY

The present study addresses the capability of a large set of shock-capturing schemes to recover the basic interactions between acoustic, vorticity and entropy in a direct numerical simulation (DNS) framework. The basic dispersive and dissipative errors are first evaluated by considering the advection of a Taylor vortex in a uniform flow. Two transonic cases are also considered. The first one consists of the interaction between a temperature spot and a weak shock. This test emphasizes the capability of the schemes to recover the production of vorticity through the baroclinic process. The second one consists of the interaction of a Taylor vortex with a weak shock, corresponding to the framework of the linear theory of Ribner. The main process in play here is the production of an acoustic wave. The results obtained by using essentially non-oscillatory (ENO), total variation diminishing (TVD), compact-TVD and MUSCL schemes are compared with those obtained by means of a sixth-order accurate Hermitian scheme, considered as reference. The results are as follows; the ENO schemes agree pretty well with the reference scheme. The second-order accurate Upwind-TVD scheme exhibits a strong numerical diffusion, while the MUSCL scheme behavior is very sensitive to the value on the parameter β in the limiter function minmod. The compact-TVD schemes do not yield improvement over the standard TVD schemes. Copyright © 2000 John Wiley & Sons, Ltd.

KEY WORDS: acoustic wave propagation; CFD; DNS; high-order shock-capturing scheme; vorticity production

1. INTRODUCTION

Direct numerical simulation (DNS) is a powerful tool for performing fine analysis of flow dynamics [1] since all the scales of the velocity field are represented in the simulation. The

* Correspondence to: CNRS, Laboratoire d'Informatique pour la Mécanique les Sciences de l'Ingénieur (CNRS-UPR 3251), BP 133, F-91403 Orsay Cedex, France.

Received November 1998
Revised August 1999

quality of the results depends only on the capability of the numerical scheme and the computational grid to capture the governing dynamical process. While non-dissipative high-order accurate schemes (spectral, Padé) have been identified as suitable tools for DNS, the potential value of high-order intrinsically dissipative schemes originally designed to capture discontinuity remains to be assessed.

The definition of DNS has to be revisited when dealing with shocks. DNS was originally defined within the framework of incompressible flows, as a simulation representing (i.e. without any model) all the relevant velocity scales of the flow. The presence of a shock introduce another length scale, the shock width δ, which is much smaller than the smallest velocity scale in realistic non-rarefied cases. Two families of simulation can then be distinguished: the fully resolved simulations (FRS), where all the scales, including the internal dynamics of the shock, are directly resolved [2], and direct numerical simulations, where only the scales associated with the velocity field are resolved, while the internal dynamics of the shock are not represented. The shock is then to be captured by using an *ad hoc* scheme with discontinuity-capturing features.

The paper is an attempt to evaluate existing schemes in practical situations. Such an analysis goes beyond theoretical analysis, and is carried out for almost all the recent high-order schemes. Hopefully, it should provide benchmark results and guidelines for the development of improved numerical schemes. The present study is a first step towards full understanding of the interaction between numerical error and elementary physical mechanisms. It focuses on the capability of numerical schemes to recover basic interactions between acoustic, vorticity and entropy, as defined by Kovasznay [3]. Basically, these tests emphasize the errors induced by performing DNS instead of FRS. The basic dispersive and dissipative errors are evaluated by considering the advection of a Taylor vortex in a uniform flow, which is an elementary test case representative of the problem of the conservation of vorticity when simulating far field wakes. Two transonic cases are also considered. The first one concerns the interaction between a temperature spot and a weak shock, which enlightens the capability of schemes to recover the creation of vorticity through the baroclinic process. This process is important when dealing with the creation of turbulence in a combustion chamber. The second test case concerns the interaction of a Taylor vortex with a weak shock, corresponding to the framework of the linear theory of Ribner [4]. The main process in play here is the production of an acoustic wave.

Four classes of shock-capturing schemes are considered: schemes based on total variation diminishing property (TVD schemes); monotonic upstream scheme for conservation laws (MUSCL schemes); compact schemes and essentially non oscillatory schemes (ENO schemes).

Governing equations and numerical schemes are presented in Section 2. Results obtained for the three selected test cases are discussed in Section 3. Conclusions are drawn in Section 4.

2. NUMERICAL APPROACH

2.1. Basic equations

This study is limited to the calculation of two-dimensional free flows. The governing equations are the unsteady compressible Navier–Stokes equations. Written in Cartesian co-ordinates and expressed using non-dimensional variables, they read

$$\frac{\partial Q}{\partial t}+\frac{\partial F}{\partial x}+\frac{\partial G}{\partial y}+\frac{\partial F_{\mathrm{v}}}{\partial x}+\frac{\partial G_{\mathrm{v}}}{\partial y}=0 \tag{1}$$

where t is the dimensionless time; x and y are the streamwise and the vertical directions respectively; the solution vector Q is based on the conservative variables; F and G are the convective fluxes; F_{v} and G_{v} stand for the viscous fluxes,

$$Q=\begin{bmatrix}\rho\\ \rho u\\ \rho v\\ \rho E\end{bmatrix},\qquad F=\begin{bmatrix}\rho u\\ \rho u^2+P\\ \rho uv\\ \rho uE+uP\end{bmatrix},\qquad G=\begin{bmatrix}\rho v\\ \rho uv\\ \rho v^2+P\\ \rho vE+vP\end{bmatrix}$$

$$F_{\mathrm{v}}=\begin{bmatrix}0\\ \sigma_{11}\\ \sigma_{12}\\ u\sigma_{11}+v\sigma_{12}+\Phi_1\end{bmatrix},\qquad G_{\mathrm{v}}=\begin{bmatrix}0\\ \sigma_{12}\\ \sigma_{22}\\ u\sigma_{12}+v\sigma_{22}+\Phi_2\end{bmatrix}$$

where ρ is the density, u, v are the velocity components in the x- and y-directions and E is the total energy per unit of mass. The stress tensor and the heat flux components are given by

$$\sigma_{ij}=-2\frac{\mu}{Re_0}\left(S_{ij}-\frac{1}{3}S_{kk}\delta_{ij}\right) \tag{2}$$

$$\Phi_i=\frac{-\mu}{(\gamma-1)Re_0\,Pr_0\,M_0^2}\frac{\partial T}{\partial x_i} \tag{3}$$

where S_{ij} stands for the strain rate tensor,

$$S_{ij}=\frac{1}{2}\left(\frac{\partial u_i}{\partial x_j}+\frac{\partial u_j}{\partial x_i}\right)$$

As usual, T and P denote the temperature and the pressure respectively. They are related to the conservative variables by using an equation of state of a perfect gas

$$P=(\gamma-1)\left[\rho E-\frac{1}{2}\frac{(\rho u)^2+(\rho v)^2}{\rho}\right] \tag{4}$$

$$T=\gamma M_0^2\frac{P}{\rho} \tag{5}$$

For the sake of simplicity, the study is restricted to ideal gas with constant specific heat ratio ($\gamma = 1.4$), constant viscosity coefficient ($\mu = \mu(T_0)$) and constant Prandtl number ($Pr_0 = 0.7$). The Reynolds number (Re_0) is based on the reference values of the density (ρ_0), velocity (V_0) and length scale (L_0). $M_0 = V_0/(\gamma R T_0)$ is the Mach number (R is the constant of the gas and T_0 is the reference temperature).

2.2. Time integration

To emphasize the differences induced by spatial discretizations, all the calculations have been performed by using the same time integration procedure. The governing equations (1) are recast in the following abridged form:

$$\frac{\partial Q}{\partial t} = \mathscr{L}(Q) \tag{6}$$

The time integration of (6) is performed by means of a third-order accurate TVD Runge–Kutta method proposed by Shu and Osher [5]

$$\begin{aligned} Q_0 &= Q^n \\ Q_1 &= Q_0 + \Delta t\, \mathscr{L}(Q_0) \\ Q_2 &= \frac{3}{4} Q_0 + \frac{1}{4} Q_1 + \frac{1}{4} \Delta t\, \mathscr{L}(Q_1) \\ Q_3 &= \frac{1}{3} Q_0 + \frac{2}{3} Q_2 + \frac{2}{3} \Delta t\, \mathscr{L}(Q_2) \\ Q^{(n+1)} &= Q_3 \end{aligned} \tag{7}$$

where Δt is the time step and Q^n denotes the vector of the conservative variables evaluated at time $n \cdot \Delta t$. The main purpose of this study is to compare the numerical error associated with the numerical treatment of the convective flux, assuming that the time integration error remains (almost) identical. To this end, all the calculations presented herein have been obtained by considering only Courant–Friedrich–Lewy (CFL) number = 0.5, which corresponds to a nearly optimal value for the considered Runge–Kutta scheme. We checked that this value ensures a good representation of all the time scales of the flows considered.

2.3. Spatial discretization

In the following, a discrete quantity $(\cdot)$ estimated at a grid point $x_i = i \cdot \Delta x$, $y_j = j \cdot \Delta y$ and at time $t = n \cdot \Delta t$ is referred to as $(\cdot)_{ij}^n$. Five spatial discretizations, based on high-order accurate approximations, have been employed.

2.3.1. Hermitian compact scheme. To obtain reference solutions by performing FRS on refined meshes, a centered sixth-order accurate Hermitian compact scheme is used. The first-order derivatives ($F' = \partial F/\partial x$) of a function ($F$) are estimated using the following relation:

$$\beta(F'_{i-2} + F'_{i+2}) + \alpha(F'_{i-1} + F'_{i+1}) + F'_i = \frac{c}{6\cdot\Delta x}(F_{i+3} - F_{i-3}) + \frac{b}{4\cdot\Delta x}(F_{i+2} - F_{i-2}) + \frac{a}{2\cdot\Delta x}(F_{i+1} - F_{i-1}) \tag{8}$$

For sixth-order accuracy, the values of the constants are

$$\alpha = \frac{1}{3}, \qquad \beta = 0, \quad a = \frac{14}{9}, \qquad b = \frac{1}{9}, \qquad c = 0$$

On the boundaries, the following third-order accurate upwind scheme is used to preserve the tridiagonal structure of the implicit operator:

$$F'_1 + 2\cdot F'_2 = \frac{1}{\Delta x}\left(\frac{-15}{6}F_1 + 2\cdot F_2 + \frac{1}{2}F_3\right) \tag{9}$$

For the second-order derivatives ($f'' = \partial^2 f/\partial x^2$), a similar scheme is applied

$$\beta(f''_{i-2} + f''_{i+2}) + \alpha(f''_{i-1} + f''_{i+1}) + f''_i = \frac{c}{9\cdot\Delta x^2}(f_{i+3} - 2\cdot f_i + f_{i-3}) + \frac{b}{4\cdot\Delta x^2}(f_{i+2} - 2\cdot f_i + f_{i-2}) + \frac{a}{2\cdot\Delta x^2}(f_{i+1} - 2\cdot f_i + f_{i-1}) \tag{10}$$

The sixth-order accuracy is achieved using

$$\alpha = \frac{2}{11}, \qquad \beta = 0, \qquad a = \frac{12}{11}, \qquad b = \frac{3}{11}, \qquad c = 0$$

On the boundaries, a third-order accurate upwind scheme is employed

$$f''_1 + 11f''_2 = \frac{1}{\Delta x^2}(13f_1 - 27f_2 + 15f_3 - f_4) \tag{11}$$

The governing equations (1) are solved by applying these one-dimensional schemes (8)–(11) in each direction. The resulting tri-diagonal systems are solved directly, using the Thomas algorithm by means of an LU factorization.

2.3.2. Upwind TVD scheme. Let us consider first an explicit upwind TVD scheme for the discretization of Equation (1)

$$\left(\frac{\partial Q}{\partial t}\right)_{ij} = -\frac{1}{\Delta x}\left[\bar{F}^n_{i+1/2,j} - \bar{F}^n_{i-1/2,j} + \bar{F}^n_{v_{i+1/2,j}} - \bar{F}^n_{v_{i-1/2,j}}\right]$$

$$-\frac{1}{\Delta y}\left[\bar{G}^n_{i,j+1/2} - \bar{G}^n_{i,j-1/2} + \bar{G}^n_{v_{i,j+1/2}} - \bar{G}^n_{v_{i,j-1/2}}\right] \tag{12}$$

The discretization of the convective terms is based on a Roe's approximate Riemann solver [6], together with an upwind TVD scheme, developed by Harten [7] and Yee [8]. The numerical flux $\bar{F}_{i+1/2,j}$ is expressed as

$$\bar{F}_{i+1/2,j} = \frac{1}{2}\left(F_{i+1,j} + F_{i,j} - R_{x_{i+1/2,j}}\Phi_{x_{i+1/2,j}}\right) \tag{13}$$

where $\Phi_{x_{i+1/2,j}}$ is a 4×4 matrix. To ensure that the scheme is a second-order accurate upwind TVD scheme, the $\phi^l_{x_{i+1/2,j}}$ elements must be written [7,9] in the following form:

$$\phi^l_{x_{i+1/2,j}} = \frac{1}{2}\left|a^l_{x_{i+1/2,j}}\right|\left(g^l_{x_{i+1,j}} + g^l_{x_{i,j}}\right) - \left|a^l_{x_{i+1/2,j}} + \gamma^l_{x_{i+1/2,j}}\right|\alpha^l_{x_{i+1/2,j}} \tag{14}$$

where $a_{x_{i+1/2,j}} = L_{x_{i+1/2,j}}(Q_{i+1,j} - Q_{i,j})$ is the forward difference of the local characteristic variables in the x-direction; $a^l_{x_{i+1/2,j}}$ are the eigenvalues; $R_{x_{i+1/2,j}}$, $L_{x_{i+1/2,j}}$ are the right and left eigenvector matrices of the Jacobian of the Euler flux $(\partial F/\partial Q)$ respectively. The parameter $\gamma_{x_{i+1/2,j}}$, given by

$$\gamma_{x_{i+1/2,j}} = \frac{1}{2}\left|a^l_{x_{i+1/2,j}}\right|\begin{cases}\dfrac{(g_{x_{i+1,j}} - g_{x_{i,j}})}{\alpha_{x_{i+1/2,j}}} & \text{if } \alpha_{x_{i+1/2,j}} \neq 0 \\ 0 & \text{if } \alpha_{x_{i+1/2,j}} = 0\end{cases}$$

Note that, contrary to the original scheme, no entropic parameter is used as we look for unsteady solutions of the equations. The limiter that gives a second-order accurate TVD scheme is the classic Van-Leer Harmonic function [10]

$$g^l_{x_{i,j}} = \frac{(\alpha^l_{x_{i+1/2,j}} \cdot \alpha^l_{x_{i-1/2,j}} + |\alpha^l_{x_{i+1/2,j}} \cdot \alpha^l_{x_{i-1/2,j}}|)}{(\alpha^l_{x_{i+1/2,j}} + \alpha^l_{x_{i-1/2,j}})} \tag{15}$$

To estimate the values at the mid-point $(i+1/2, j)$ and to ensure that the numerical flux $(\bar{F})$ is consistent with F, the classic mass-weighted average is introduced by Roe [6]. The numerical flux $(\bar{G}^n_{i,j+1/2})$ in the y-direction is expressed following the same formulation as in the x-direction.

The diffusive fluxes ($\bar{F}_v$ and $\bar{G}_v$) are discretized using a second-order accurate differencing scheme.

2.3.3. Compact TVDM scheme. To increase the order of accuracy of the previous scheme, a compact shock-capturing scheme, based on TVD in mean (TVDM) approximation was implemented, as proposed by Yee [11]

$$A_x A_y\left(\frac{\partial Q}{\partial t}\right)_{ij} = -\frac{1}{\Delta x} A_y[\bar{F}^n_{i+1/2,j} - \bar{F}^n_{i-1/2,j} + \bar{F}^n_{v_{i+1/2,j}} - \bar{F}^n_{v_{i-1/2,j}}] - \frac{1}{\Delta y} A_x[\bar{G}^n_{i,j+1/2} - \bar{G}^n_{i,j-1/2} + \bar{G}^n_{v_{i,j+1/2}} - \bar{G}^n_{v_{i,j-1/2}}] \tag{16}$$

where, to ensure fourth-order accuracy, the coefficients of the Hermitian matrices (A_x and A_y) are

$$A_x(\Phi)_{i,j} = \frac{1}{24}(\Phi_{i-1,j} + 22\Phi_{i,j} + \Phi_{i+1,j}) \tag{17}$$

$$A_y(\Phi)_{i,j} = \frac{1}{24}(\Phi_{i,j-1} + 22\Phi_{i,j} + \Phi_{i,j+1}) \tag{18}$$

In this TVDM compact scheme, the numerical Euler fluxes $\bar{F}_{i+1/2,j}$ and $\bar{G}_{i,j+1/2}$ are estimated using the previous TVD approach (13). The diffusive fluxes $\bar{F}_{v_{i+1/2,j}}$ and $\bar{G}_{v_{i,j+1/2}}$ involve spatial derivatives of velocity that have been estimated also by a fourth-order accurate compact scheme, written at the mid-point, using for instance

$$A_x\left(\frac{\partial U}{\partial x}\right)_{i+1/2,j} = \frac{1}{\Delta x}(U_{i+1,j} - U_{i,j}) \tag{19}$$

where matrix (A_x) is defined by Equation (17).

2.3.4. MUSCL-TVD scheme. The convective numerical flux functions $\bar{F}_{i+1/2,j}$ and $\bar{G}_{i,j+1/2}$ are also estimated using a MUSCL approach, based on an approximate Riemann solver. Using the local characteristic approach [12], the upwind MUSCL scheme reads

$$\bar{F}_{i+1/2,j} = \frac{1}{2}(F(Q^R_{i+1/2,j}) + F(Q^L_{i+1/2,j}) - R_{x_{i+1/2,j}}\Phi_{x_{i+1/2,j}}) \tag{20}$$

Spurious oscillations are eliminated by using a 'slope' limiter applied to the conservative variables (Q)

$$Q^R_{i+1/2,j} = Q_{i+1,j} - \frac{1}{4}[(1-\eta)\tilde{\Delta}_{i+3/2} + (1+\eta)\tilde{\tilde{\Delta}}_{i+1/2}] \tag{21}$$

$$Q^L_{i+1/2,j} = Q_{i,j} + \frac{1}{4}[(1-\eta)\tilde{\tilde{\Delta}}_{i-1/2} + (1+\eta)\tilde{\Delta}_{i+1/2}] \tag{22}$$

In the present calculations, a minmod 'slope' limiter was used together with $\eta = \frac{1}{3}$, leading to the definition of a third-order accurate upwind-biased scheme

$$\tilde{\Delta}_{i+1/2} = \text{minmod}(\Delta_{i+1/2}, \beta\Delta_{i-1/2}) \tag{23}$$

$$\tilde{\tilde{\Delta}}_{i+3/2} = \text{minmod}(\Delta_{i+1/2}, \beta\Delta_{i+3/2}) \tag{24}$$

where $\Delta_{i+1/2} = Q_{i+1,j} - Q_{i,j}$ and $\text{minmod}(p, q) = \text{sign}(p)\cdot\max\{0, \min[|p|, q\ \text{sign}(p)]\}$.

Two extreme values of the β coefficient have been considered: $\beta = 1$, giving the most diffusive MUSCL scheme, and $\beta = 4$ giving the most compressive one. The elements of the matrix $\Phi_{x_{i+1/2,j}}$ are written [12]

$$\phi^l_{x_{i+1/2,j}} = |a^l_{x_{i+1/2,j}}| L_{x_{i+1/2,j}}(Q^R_{i+1/2,j} - Q^L_{i+1/2,j}) \tag{25}$$

The eigenvalues $a^l_{x_{i+1/2,j}}$ and the eigenvectors matrices $R_{x_{i+1/2,j}}$, $L_{x_{i+1/2,j}}$ of $\partial F/\partial Q$ are evaluated by using the Roe average between states $Q^R_{i+1/2,j}$ and $Q^L_{i+1/2,j}$.

2.3.5. ENO schemes. Finally, ENO schemes have been employed to evaluate the Euler fluxes [5,13]. The ENO reconstruction is applied to the local characteristic variables. The Euler fluxes (in each direction) are projected onto the left eigenvectors matrices $L_{x_{i+1/2,j}}$ and $L_{y_{i,j+1/2}}$ of $(\partial F/\partial Q)_{i+1/2,j}$ and $(\partial G/\partial Q)_{i,j+1/2}$ respectively. The scalar ENO reconstruction procedure is applied to the projected fluxes [13]. The numerical Euler fluxes are obtained in the physical domain by a projection onto the right eigenvectors $R_{x_{i+1/2,j}}$ and $R_{y_{i+1/2,j}}$. The numerical Euler fluxes finally read

$$\bar{F}_{i+1/2,j} = \sum_{l=1}^{4}\left[\sum_{p=0}^{r-1}\zeta^{r,l}_p L^l_{x_{i+1/2,j}}\cdot F(Q_{i,j})R^l_{x_{i+1/2,j}}\right] \tag{26}$$

$$\bar{G}_{i,j+1/2} = \sum_{l=1}^{4}\left[\sum_{p=0}^{r-1}\zeta^{r,l}_p L^l_{y_{i,j+1/2}}\cdot G(Q_{i,j})R^l_{y_{i,j+1/2}}\right] \tag{27}$$

The eigenvectors matrices (L and R) are evaluated using the Roe average.

The generic ENO scheme

The ENO reconstruction procedure [13] is employed to choose the most regular stencil among the $r+1$ candidates (r is the order of the ENO reconstruction). After selecting the r upwind stencils using the sign of the eigenvalues $(a^l_{x_{i+1/2,j}}, a^l_{y_{i,j+1/2}})$ of $(\partial F/\partial Q)_{i+1/2,j}$, $(\partial G/\partial Q)_{i,j+1/2}$ respectively, the undivided difference table of the Euler fluxes is constructed to chose the most regular stencil. The ζ coefficients are calculated to approximate the polynomial extrapolation [13] of order $r=2m+1$

$$\bar{f}_{i+1/2} = f_{i+1/2} + \sum_{p=1}^{m} \Delta x^{2p} a_{2p} \frac{\partial^{2p}}{\partial x^{2p}} (f_{i+1/2}) + O(\Delta x)^{2m+1} \tag{28}$$

$$\bar{f}_{i+1/2} = \sum_{q=0}^{r-1} \zeta^r_q f_q \tag{29}$$

The values of ζ^r_l can be found in Shu [14].

Using this generic ENO scheme (26), the Euler fluxes derivatives are estimated with r-order of accuracy at best.

Modified ENO scheme (MENO)

Whenever the stencil used to evaluate $\bar{f}_{i+1/2}$ is different to the stencil used to evaluate $\bar{f}_{i-1/2}$ the order of accuracy decreases to $r-1$. This drawback is limited to the modified ENO (MENO) schemes [15] since these schemes select automatically the most centered stencil in smooth regions for both $\bar{f}_{i+1/2}$ and $\bar{f}_{i-1/2}$.

Weighted ENO scheme (WENO)

The generic ENO scheme needs to choose between r candidate stencils. The principle of the weighted ENO scheme is to improve the order of accuracy by using a weighted combination of the r possible stencils. The weights [16] depend on the degree of regularity of the solution. In regular regions, they can be computed to achieve $(2r-1)$th-order of accuracy, whereas in regions with discontinuities they are set to zero, leading to a standard ENO scheme. The WENO fluxes are estimated by

$$\bar{F}_{i+1/2,j} = \sum_{k=0}^{r-1} \omega_k q^r_k (F_{i+k-r+1,j}, \ldots, F_{i+k,j}) \tag{30}$$

$$\bar{G}_{i,j+1/2} = \sum_{k=0}^{r-1} \omega_k q^r_k (G_{i,j+k-r+1}, \ldots, F_{i,j+k}) \tag{31}$$

where q^r_k stands for the ENO reconstruction of the Euler fluxes for the kth stencil,

$$q^r_k (f_{i+k-r+1}, \ldots, f_{i+k}) = \sum_{p=0}^{r-1} \zeta^r_{k,p} f_p \tag{32}$$

and ω_k are the weights defined as follows:

$$\sum_{k=0}^{r-1} \omega_k = 1 \tag{33}$$

$$\omega_k = \frac{\beta_k}{r-1} \tag{34}$$

$$\beta_k = \frac{\sum_{p=0} \beta_p C_k^r}{(\varepsilon + IS_k)^2} \tag{35}$$

ε is a small positive number to avoid the denominator being zero (hereafter we set $\varepsilon = 10^{-6}$) and IS_k is a measure of the flux function regularity for the kth candidate stencil. The evaluation of the smoothness measurement (IS_k) is based on the undivided differences [16].

The C_k^r coefficients can be found in Reference [17] up to $r = 4$.

For all these ENO schemes, the diffusion terms are discretized by means of a second-order accurate central differencing scheme.

3. RESULTS AND DISCUSSION

The simulations have been performed by using the following seven numerical schemes:

- A sixth-order accurate Hermitian scheme (referred to as Hermit 6)
- A second-order accurate upwind TVD scheme using a Van-Leer harmonic limiter function, based on a Roe–Riemann solver (referred to as TVD-HY 2)
- A third-order accurate MUSCL-TVD scheme using a minmod limiter function, based on a Roe–Riemann solver (referred to as MUSCL 3)
- A fourth-order accurate compact TVDM scheme using a Van-Leer harmonic limiter function, based on a Roe–Riemann solver (referred to as CP-TVDM 4).
- A third-order accurate ENO scheme, based on a Roe–Riemann solver (referred to as ENO 3).
- A fourth-order accurate ENO scheme, based on a Roe–Riemann solver (referred to as MENO 4)
- A fifth-order accurate WENO scheme, based on a Roe–Riemann solver (referred to as WENO 5)

Note that for each scheme, the accuracy order we have reported is the best they can achieve.

3.1. Advection of a vortex

In the present test case our goal is to evaluate the diffusive or dispersive property of each scheme. All calculations have been performed on the same configuration with the same initial data.

3.1.1. Flow configuration. The physical domain is the square $[0, L_0] \times [0, L_0]$. By using L_0 a as reference length scale, the computations are performed on the dimensionless domain $[0, 1] \times [0, 1]$. An isolated Taylor vortex is initially superimposed to a uniform flow with a Mach number $M_0 = 0.8$ and a Reynolds number $Re = 10^4$. The tangential velocity is given by

$$V_\theta(r) = C_1 r \cdot \mathrm{e}^{-C_2 r^2} \tag{36}$$

with

$$C_1 = \frac{U_c}{r_c}\,\mathrm{e}^{1/2}, \qquad C_2 = \frac{1}{2r_c^2}, \qquad r = \sqrt{(x - x_0)^2 + (y - y_0)^2}$$

We set $r_c = 0.075$ and $U_c = 0.3$. Following these values, the radius of the viscous core is $\frac{1}{2}$. The initial position of the vortex center is $x_0 = \frac{1}{2},\ y_0 = \frac{1}{2}$.

Periodic boundary conditions are applied in both directions (x, y). Two uniform grids are employed: a coarse grid with 100×100 points and a fine one with 200×200 points. The CFL number is set to 0.5, corresponding to a dimensionless time step $\Delta t = 1 \times 10^{-3}$ on the fine grid and $\Delta t = 2 \times 10^{-3}$ on the coarse grid.

3.1.2. Results. The simulation is performed over a dimensionless time $t = 5$, corresponding to the advection of the vortex over five length scales (L_0). The conservative quantities are recorded at each integer time $(t = 1, 2, 3, 4, 5)$ when the center of the vortex coincides with the center of the domain owing to the periodic boundary condition.

Owing to the effects of both molecular viscosity and numerical diffusion, the radius of the viscous core is a growing function of time. This is illustrated in Figure 1, where the distribution of the vertical component (v) of the velocity on the centerline of the domain $(y = \frac{1}{2})$ at a dimensionless time $t = 5$ is compared with the initial distribution. This effect can also be seen on the longitudinal distribution of the static pressure (P) at a dimensionless time $t = 5$ on the centerline of the domain $(y = \frac{1}{2})$ (Figure 2). The pressure defect is located at the center of the vortex. The more dissipative the scheme the less important the pressure defect (Figure 2).

The results obtained by using the sixth-order accurate Hermitian scheme (Hermit 6) on the fine grid (200×200) are taken as the reference values. Note in Figures 1 and 2 that, on the fine grid, the shock-capturing schemes give results in good agreement with the Hermit-6, except MUSCL-3 using $\beta = 1$, which exhibits large discrepancies. Even though this scheme is a 'biased' third-order accurate scheme, it gives the most important numerical diffusion. Improvements are obtained by using $\beta = 4$. Nevertheless, all the shock-capturing schemes exhibit large discrepancies on the coarse grid when compared with the Hermit-6 results (Figures 1 and 2). Moreover, note on Figures 1 and 2 that, owing to the upwinding, the distributions of both v and P obtained by means of the TVD schemes are not symmetric with respect to the abscissa $x_0 = \frac{1}{2}$.

To get a finer analysis of the capability of each scheme to reproduce the vortex advection, we make a zoom around the maximum of v at a dimensionless time $t = 5$ (Figures 3 and 4). The sixth-order accurate Hermitian scheme (Hermit-6) is not sensitive to the mesh refinement since the differences are less than 0.1 per cent between both grids (see Figures 3 and 4). The

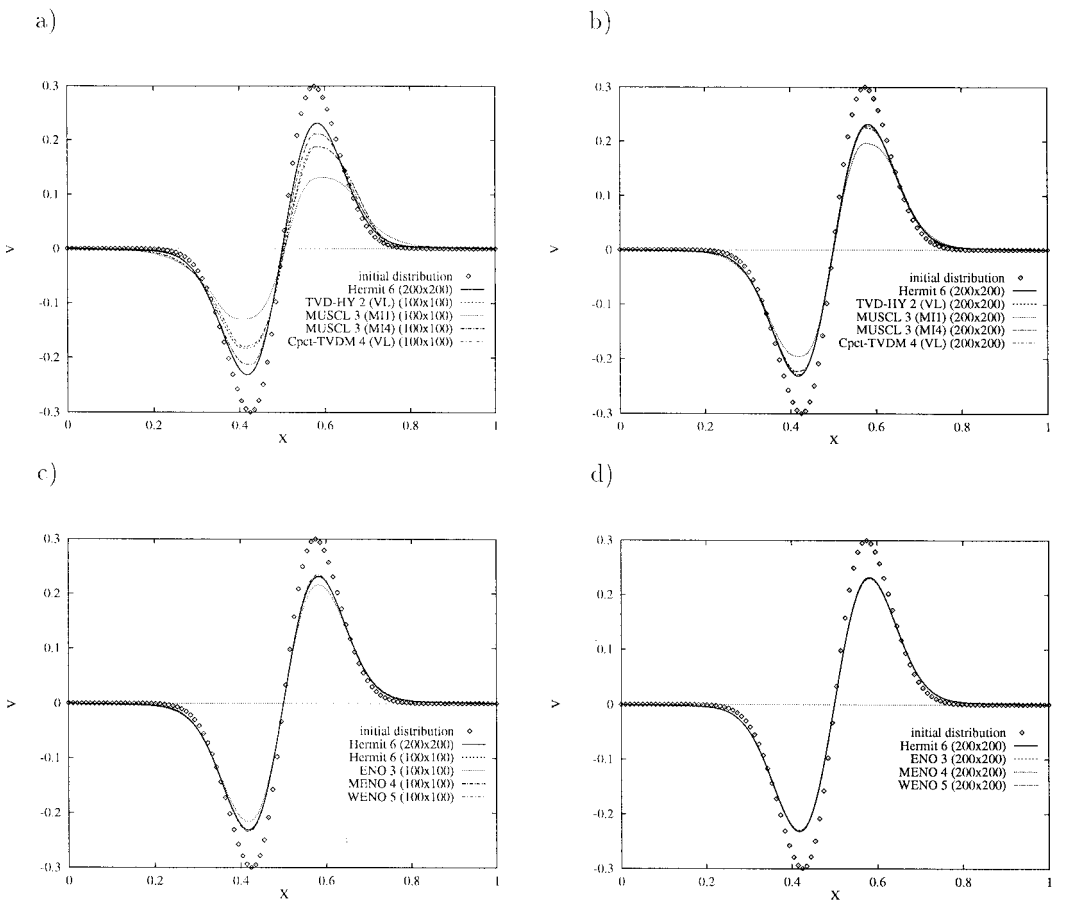

Figure 1. Advection of a vortex ($Re = 10^4$, $M_0 = 0.8$): vertical velocity (v) at $t = 5$ as a function of x on line $y = \frac{1}{2}$. (a) TVD schemes on the coarse grid (100×100); (b) TVD schemes on the fine grid (200×200); (c) ENO schemes on the coarse grid (100×100); (d) ENO schemes on the fine grid (200×200).

distributions calculated using shock-capturing schemes are compared with the Hermit-6 results in Figures 3 and 4. The results of MUSCL-3 with $\beta = 1$ (MUSCL3(MI1)) have not been plotted since its numerical diffusion is too important.

The TVD-HY scheme using the Van-Leer Harmonic limiter function gives large differences compared with the Hermit-6 results due to the numerical diffusion, especially on the coarse grid (Figures 1(left), 2(left), 3(a) and 4(a)). Results on the fine grid are in closer agreement with the Hermit-6 distribution (Figures 1(right), 2(right), 3(b) and 4(b)). Compact TVDM-4 (VL) exhibits a disappointing behavior since it is comparable with the second-order Upwind-TVD and no improvement is observed using the compact approach on both grids (Figures 1; 3(a) and (b), 2; and 4(a) and (b)). This behavior is attributed to the limiter function, which

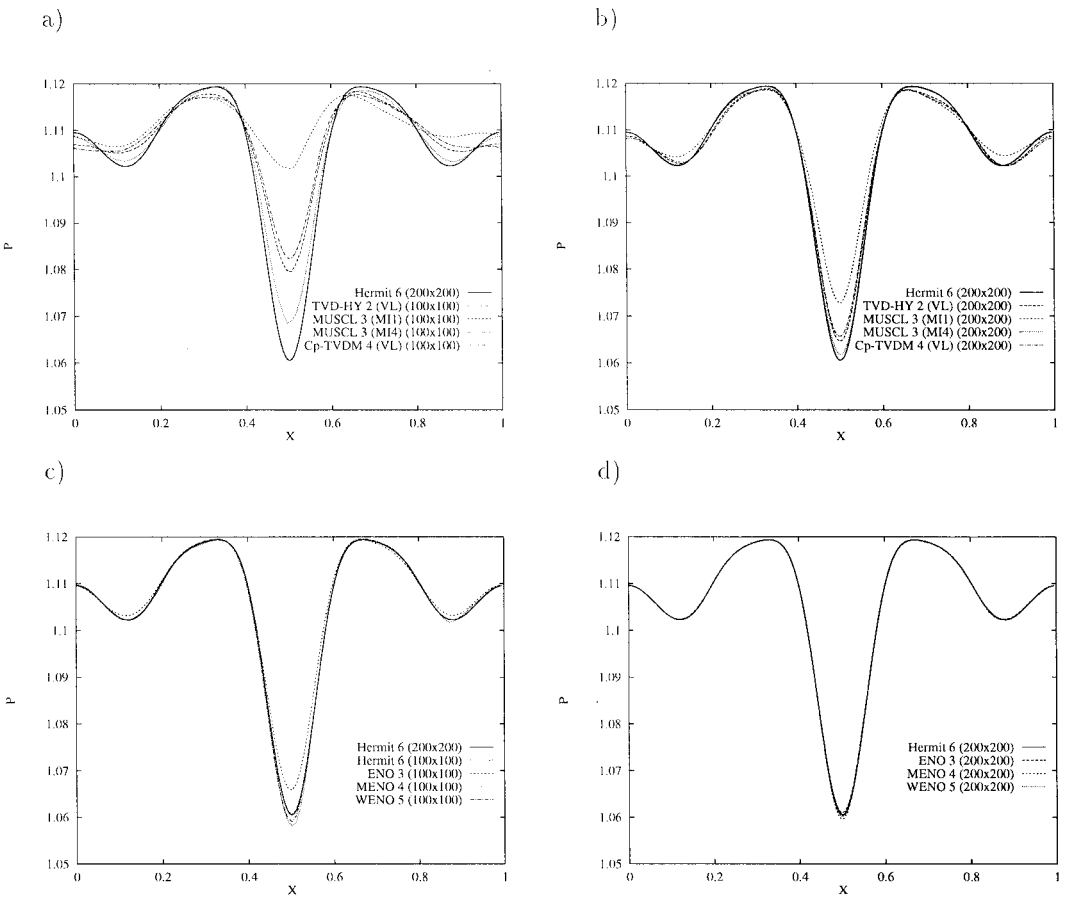

Figure 2. Advection of a vortex ($Re = 10^4$, $M_0 = 0.8$): static pressure (P) at $t = 5$ as a function of x on line $y = \frac{1}{2}$. (a) TVD schemes on the coarse gird (100×100); (b) TVD schemes on the fine grid (200×200); (c) ENO schemes on the coarse grid (100×100); (d) ENO schemes on the fine grid (200×200).

decreases by 1 the order of accuracy of the Euler fluxes in the right-hand side of (16). Then, the resulting compact scheme is no longer fourth-order accurate in space. Additional tests (not shown here) have been performed using the compact approach applied to a centered scheme, to evaluate the right-hand side of (16), leading to results very similar to those of the Hermit-6 scheme. This confirms the role played by the limiter function. MUSCL-3, using a minmod limiter function with $\beta = 4$ (MI4), gives results in better agreement with the reference values than the basic TVD-HY scheme (Figures 1; 3(a) and (b), 2; and 4(a) and (b)). The MUSCL-3(MI4) results are comparable with those obtained by means of the basic ENO-3 scheme. Both schemes exhibit slightly diffusive behavior (Figures 1; 3, 2; and 4). Improvements have been obtained by using modified and weighted ENO schemes (MENO-4 and WENO-5)

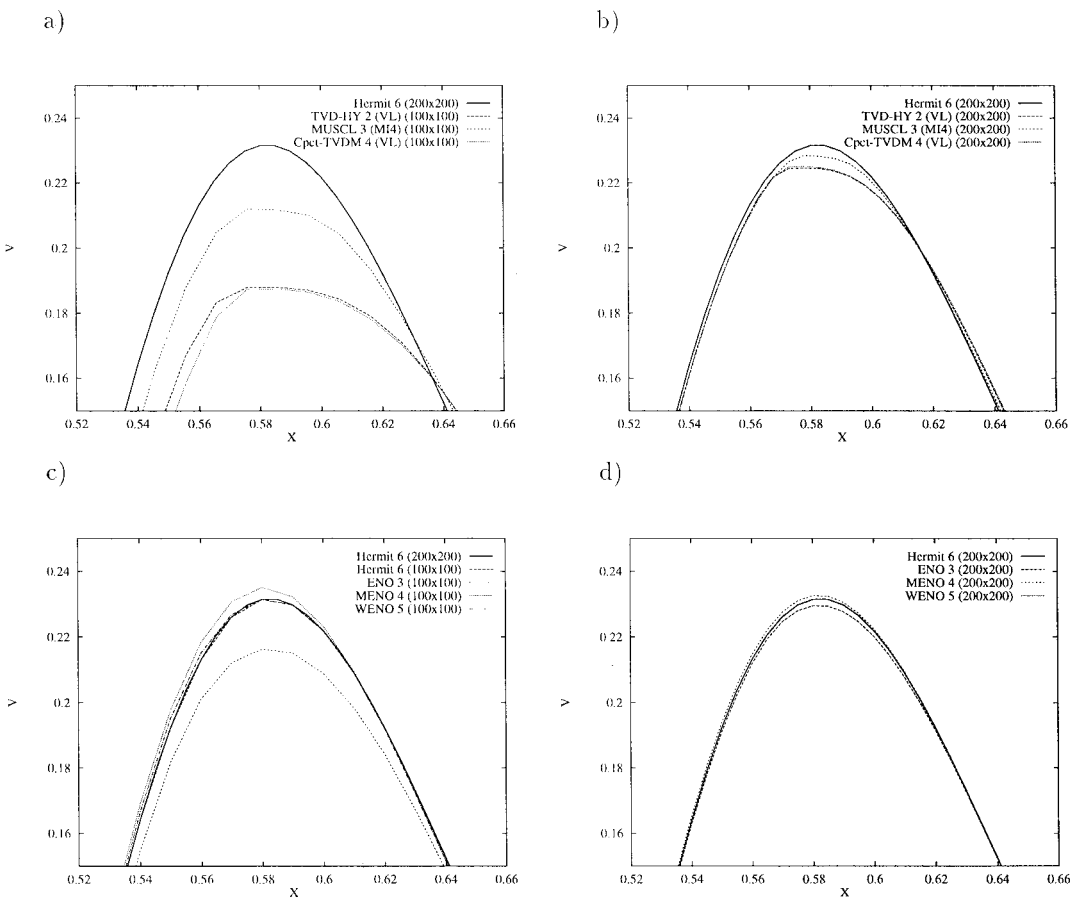

Figure 3. Zoom around the center of the vortex at a dimensionless time $t = 5$ of the longitudinal distribution (along the line $y = \frac{1}{2}$) of the vertical velocity (v). (a) TVD schemes on the coarse grid (100×100); (b) TVD schemes on the fine grid (200×200); (c) ENO schemes on the coarse grid (100×100); (d) ENO schemes on the fine grid (200×200).

(Figures 3(c) and (d), and 4(c) and (d)). The MENO-4 scheme seems to exhibit some anti-diffusive behavior, since the maximum of v is overestimated and, consequently, the minimum of pressure is underestimated (Figures 3(c) and (d) and 4(c) and (d)). The best agreement with the reference is provided by the WENO-5 scheme. Nevertheless, this scheme exhibits also a slight anti-diffusive behavior, mainly on the coarse grid (Figures 3(c) and (d) and 4(c) and (d)). However, this trend is less important than for the MENO-4 scheme.

The comparisons between the seven numerical schemes are now performed on the time evolution of the maximum (over the computational domain) of the vertical velocity (v) and the minimum of the pressure (P), when the center of the vortex coincides with the center of the

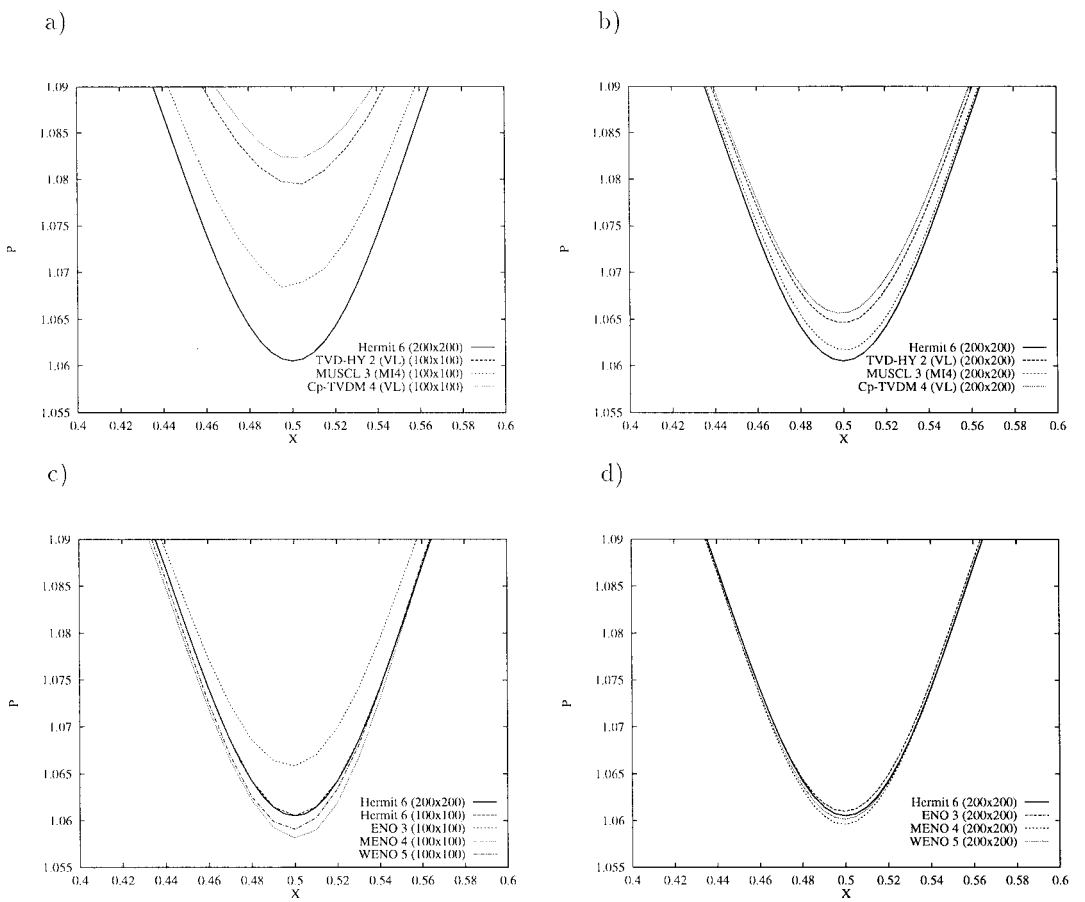

Figure 4. Zoom around the center of the vortex at $t = 5$ of the longitudinal distribution (along the line $y = \frac{1}{2}$) of the the static pressure (P). (a) TVD schemes on the coarse grid (100×100); (b) TVD schemes on the fine grid (200×200); (c) ENO schemes on the coarse grid (100×100); (d) ENO schemes on the fine grid (200×200).

domain (i.e. $t = 1, 2, 3, 4, 5$). The maximum of v and the minimum of P, on both the fine (200×200) and the coarse (100×100) grids are presented in Tables I and II respectively. Relative errors with respect to the Hermitian scheme on the finer grid are also given.

The sixth-order accurate Hermitian scheme (Hermit-6) is not sensitive to the mesh refinement since the maximum in time of the error on the coarse grid, compared with the fine grid, is less than 0.1 per cent for the maximum of v and less than 0.5 per cent for the minimum of P (Tables I and II). The most diffusive scheme is the biased third-order accurate MUSCL scheme using $\beta = 1$, which gives a maximum error up to 43 per cent for the maximum of v on the coarse grid (Table I). Large improvements are obtained using the coefficient value $\beta = 4$

Table I. Advection of a concentrated vortex ($Re = 10^4$, $M_0 = 0.8$): time evolution of the maximum of the vertical velocity component (v) in the computational domain.

Schemes	$T = 1$		$T = 2$		$T = 3$		$T = 4$		$T = 5$	
	Max (v)	Error (%)	Max (v)	Error (%)	Max (v)	Error (%)	Max (v)	Error (%)	Max (v)	Error (%)
HERMIT-6 (200×200)	0.27855	0.000	0.26432	0.000	0.25060	0.000	0.24412	0.000	0.23163	0.000
HERMIT-6 (100×100)	0.27853	−0.007	0.26431	−0.004	0.25059	−0.004	0.24409	−0.012	0.23140	−0.099
TVD-HY-2 (VL) (200×200)	0.27472	−1.375	0.25902	−2.005	0.24444	−2.458	0.23690	−2.958	0.22461	−3.031
TVD-HY-2 (VL) (100×100)	0.26044	−6.502	0.24270	−8.179	0.22089	−11.856	0.20505	−16.004	0.18787	−18.892
MUSCL-3(MI1) (200×200)	0.26399	−5.227	0.24280	−8.142	0.22292	−11.045	0.21045	−13.792	0.19656	−15.141
MUSCL-3(MI1) (100×100)	0.23094	−17.092	0.20126	−23.857	0.17389	−30.611	0.15220	−37.654	0.13105	−43.423
MUSCL-3(MI4) (200×200)	0.27732	−0.442	0.26232	−0.757	0.24847	−0.850	0.24137	−1.126	0.22914	−1.075
MUSCL-3(MI4) (100×100)	0.26995	−3.087	0.25284	−4.343	0.23457	−6.397	0.22443	−8.066	0.21339	−7.875
ENO-3 (200×200)	0.27646	−0.750	0.26331	−0.382	0.25008	−0.208	0.24316	−0.393	0.22949	−0.924
ENO-3 (100×100)	0.27472	−1.375	0.26157	−1.040	0.24263	−3.180	0.23297	−4.567	0.21967	−5.163
Cpct-TVDM-4 (200×200)	0.27537	−1.142	0.25994	−1.657	0.24507	−2.207	0.23758	−2.679	0.22502	−2.854
Cpct-TVDM-4 (100×100)	0.26237	−5.809	0.24527	−7.207	0.22397	−10.626	0.20780	−14.879	0.18817	−18.763
MENO-4 (200×200)	0.27913	−0.208	0.26489	0.216	0.25139	0.315	0.24517	0.430	0.23276	0.488
MENO-4 (100×100)	0.28033	−0.639	0.26546	0.431	0.25358	1.189	0.24705	1.200	0.23511	1.502
WENO-5 (200×200)	0.27852	−0.011	0.26433	0.004	0.25063	0.012	0.24417	0.020	0.23168	0.022
WENO-5 (100×100)	0.27798	−0.205	0.26389	−0.163	0.25055	−0.020	0.24423	0.045	0.23145	−0.078

Table II. Advection of a concentrated vortex ($Re = 10^4$, $M_0 = 0.8$): time evloution of the minimum of the pressure (P) in the computational domain.

Schemes	$T = 1$		$T = 2$		$T = 3$		$T = 4$		$T = 5$	
	Max (P)	Error (%)	Max (P)	Error (%)	Max (P)	Error (%)	Max (P)	Error (%)	Max (P)	Error (%)
HERMIT-6 (200×200)	1.01276	0.0000	1.01789	0.0000	1.01964	0.0000	1.08101	0.0000	1.06052	0.0000
HERMIT-6 (100×100)	1.01276	0.0000	1.01791	0.0020	1.01964	0.0000	1.08093	−0.0074	1.06550	0.4696
TVD-HY-2 (VL) (200×200)	1.01332	0.0553	1.01931	0.1395	1.02131	0.1638	1.07984	−0.1082	1.06468	0.3923
TVD-HY-2 (VL) (100×100)	1.01631	0.3505	1.02716	0.9107	1.03154	1.1671	1.08627	0.4866	1.07838	1.6841
MUSCL-3(MI1) (200×200)	1.01617	0.3367	1.02412	0.6121	1.02827	0.8464	1.08568	0.4320	1.07276	1.1542
MUSCL-3(MI1) (100×100)	1.03010	1.7122	1.04794	2.9522	1.05797	3.7592	1.10859	2.5513	1.10142	3.8566
MUSCL-3(MI4) (200×200)	1.01325	0.0484	1.01859	0.0688	1.02042	0.0765	1.08092	−0.0083	1.06171	0.1122
MUSCL-3(MI4) (100×100)	1.01576	0.2962	1.02246	0.4490	1.02518	0.5433	1.08386	0.2636	1.06840	0.7430
ENO-3 (200×200)	1.01319	0.0425	1.01832	0.0422	1.02014	0.0490	1.08077	−0.0222	1.06066	0.0132
ENO-3 (100×100)	1.01495	0.2162	1.01915	0.1238	1.02227	0.2579	1.08123	0.0204	1.06224	0.1662
Cpct-TVDM-4 (200×200)	1.01324	0.0474	1.01946	0.1542	1.02156	0.1883	1.07939	−0.1499	1.06561	0.4800
Cpct-TVDM-4 (100×100)	1.01588	0.0.308	1.02739	0.9333	1.03235	1.2465	1.08487	0.3571	1.07949	1.7887
MENO-4 (200×200)	1.01256	−0.0197	1.01747	− 0.0413	1.01918	−0.0451	1.08110	0.0083	1.05962	−0.0849
MENO-4 (100×100)	1.01232	−0.0434	1.01712	− 0.0756	1.01860	−0.1020	1.08028	−0.0675	1.05813	−0.2254
WENO-5 (200×200)	1.01270	−0.0059	1.01776	− 0.0128	1.01948	−0.0157	1.08117	0.0148	1.06016	−0.0339
WENO-5 (100×100)	1.01246	−0.0296	1.01727	− 0.0609	1.01881	−0.0814	1.08063	−0.0352	1.05908	−0.1358

since the maximum error is reduced to less than 8 per cent on the coarse grid and about 1 per cent on the fine grid (Table I). The TVD-HY-2 and the Compact TVDM-4 schemes give comparable results. These schemes exhibit important errors on the coarse grid. TVD schemes are sensitive to grid refinement since these errors are greatly reduced on the fine grid. This grid sensitivity may come from the Van-Leer Harmonic limiter function, which overpredicts the limitation on the Euler fluxes on the coarse grid.

ENO schemes lead to very low error level when compared with TVD schemes. The ENO-3 scheme on the coarse grid gives a maximum error close to 5 per cent. This error decreases to less than 1 per cent as the resolution increases. On the fine grid, ENO-3 and MUSCL-3(MI4) give comparable results, while the ENO-3 scheme behaves slightly better on the coarse grid. The MENO approach improves the results on the coarse grid whereas an error level similar to that of the generic ENO is found on the fine mesh. The computational time is equivalent for both approaches. The WENO-5 scheme provides results in very good agreement with the Hermitian scheme on both grids (see Tables I and II).

These results demonstrate that the convection of an isolated vortex is satisfactorily predicted using a shock-capturing scheme that is at least third-order accurate in space. The best results are provided by the WENO scheme with a computational time comparable with that of the generic ENO scheme.

3.2. Interaction between a weak shock and a spot of temperature

The goal of this section is to investigate the capability of shock-capturing schemes to predict correctly the mechanisms of vorticity production during the interaction of travelling pressure waves (or shocks) with inhomogeneities of the flow [9] induced by baroclinic effects. Recall that only baroclinic effects are capable of producing vorticity in two-dimensional in viscid flows. This configuration is a basic model for the interaction of a shock with a flame. As the classical approach that is based on the linear theory of the Rayleigh–Taylor instabilities cannot take into account the non-linear mechanisms [18], DNS emerges as an attractive alternative to understanding the mechanisms of vorticity production.

The baroclinic production term reads

$$-\frac{1}{\rho^2}\nabla P \times \nabla \rho \tag{37}$$

3.2.1. Flow configuration. The flow configuration is the one studied by Pernaud-Thomas [19] in his PhD thesis. The domain has a dimension $2L_0 \times L_0$, where L_0 is chosen as the reference length scale. The dimensionless computational domain (Ω) is $[0, 2] \times [0, 1]$. The plane weak shock is located at $x_0 = 1$. The prescribed pressure jump through the shock is $\Delta P/P_\infty = 0.4$, where P_∞ is the static pressure at infinity, corresponding to a reference Mach number $M_0 = 1.1588$. The flow is initialized by using the Rankine–Hugoniot relationships. The Reynolds number, based on the reference length scale (L_0), density (ρ_0) and velocity (V_0), is $Re = 2000$. The reference density and velocity are those of the free uniform flow at infinity. Initially, the spot of temperature is superimposed to the base flow and is located upstream of the shock (see Figure 5). The spot of temperature is defined as

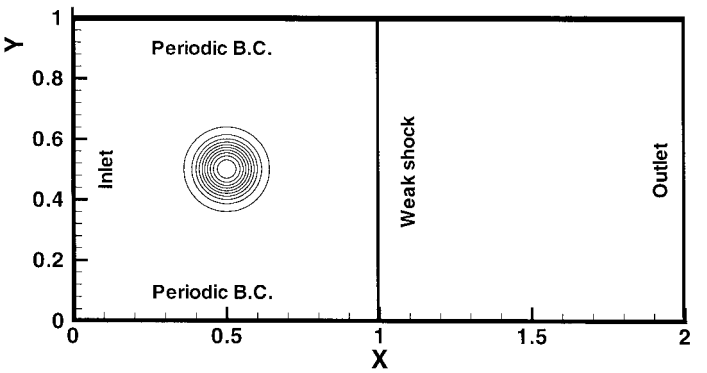

Figure 5. Computational domain, boundary conditions and initial density field.

$$\frac{\Delta T(r)}{T_0} = \frac{1}{\alpha^4}(r^2 - \alpha^2)^2 \, \mathrm{e}^{-r^2/\sigma^2} \tag{38}$$

with $\alpha = 7$, $\sigma = 0.07$, and where $r = \sqrt{(x - x_0)^2 + (y - y_0)^2}$ and $x_0 = \frac{1}{2}$, $y_0 = \frac{1}{2}$ are the co-ordinates of the initial location of the center of the spot. The perturbation of temperature is supposed to be isobaric.

On the upstream boundary ($x = 0$), as the inflow is supersonic all the conservative quantities are prescribed. On the outflow boundary ($x = 2$) we proceed as follows:

- for the TVD and MUSCL schemes, the governing equations are projected onto the characteristic directions and non-reflecting conditions are applied in the streamwise direction.
- for the ENO schemes, ghost cells are added, on which the condition $\partial/\partial x = 0$ is prescribed to conserve the order of accuracy of the scheme.
- for the Hermitian scheme, first order extrapolations of the conservative variables are employed.

Periodic boundary conditions are applied on the upper and lower boundaries. Two uniform grids are used: a coarse grid with 101×51 points ($\Delta x = \Delta y = 0.02$) and a fine grid with 201×101 points ($\Delta x = \Delta y = 0.01$). To obtain a reference solution, a FRS calculation was performed on a very fine grid (801×101), using the Hermit-6 scheme (as in Reference [2]), with about ten points within the shock wave.

The calculations have been performed over a dimensionless time equal to 1, using a Courant number CFL = 0.5, corresponding to a dimensionless time step equal to $\Delta t = 4 \times 10^{-3}$ on the coarse grid and $\Delta t = 2 \times 10^{-3}$ on the fine grid.

3.2.2. Results. As the spot of temperature is convected through the shock, the sum over the computational domain (Ω) of the modulus of both the vorticity and the baroclinic torque (37) are computed

$$\int_{\Omega} |\omega| \, d\Omega \tag{39}$$

$$\int_{\Omega} \left| \frac{\nabla P \times \nabla \rho}{\rho^2} \right| d\Omega \tag{40}$$

We first present the reference solution obtained by means of the sixth-order accurate Hermitian scheme. The time histories of the integral quantities (39) and (40) are plotted in Figures 6 and 7. At the initial time ($t = 0$), the vorticity and the baroclinic torque are zero (Figures 6 and 7). At a dimensionless time $t = 0.3$, the temperature spot starts to interact with the shock wave (Figures 6 and 7). The maximum of the production of vorticity occurs at about $t = 0.5$ when the center of the temperature spot coincides with the shock location. The isovalues of the density and pressure (Figure 8) show a modification in the curvature of the shock. The vorticity is produced within and just downstream the shock (Figure 8); the final product being a pair of counterrotating vortices. Since the initial temperature distribution is symmetric, the vorticity field is anti-symmetric with respect to the centerline $y = \frac{1}{2}$ of the domain. Low-pressure structures associated with these vortices are visible in Figure 8. As the spot is convected downstream of the weak shock, the intensity of the baroclinic torque decreases rapidly (Figure 7). At $t = 1$, the temperature spot is located close to $x = 1.4$ but still interacts with the shock as shown in (Figure 9) as the shock is bent. The production of

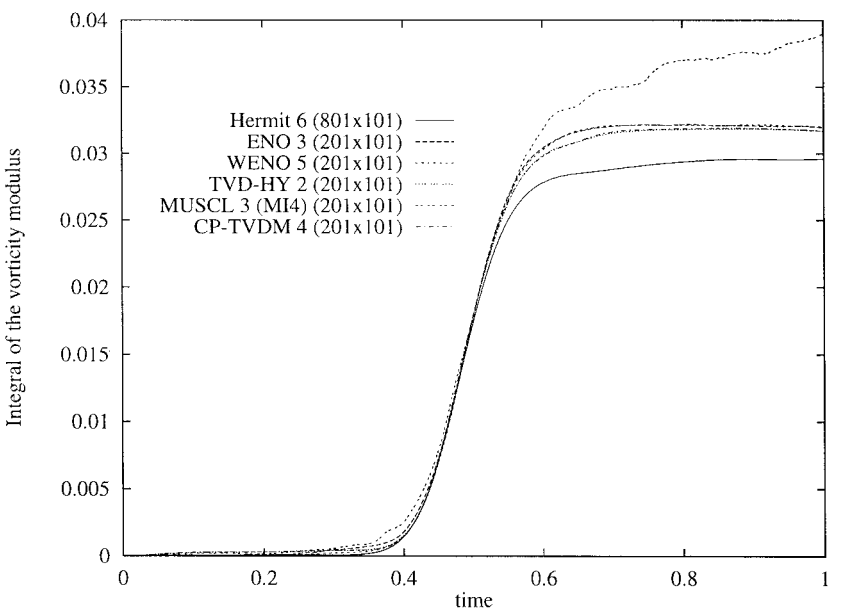

Figure 6. Time history of the integral over the computational domain of $|\omega|$ obtained by different schemes on the fine grid (201×101).

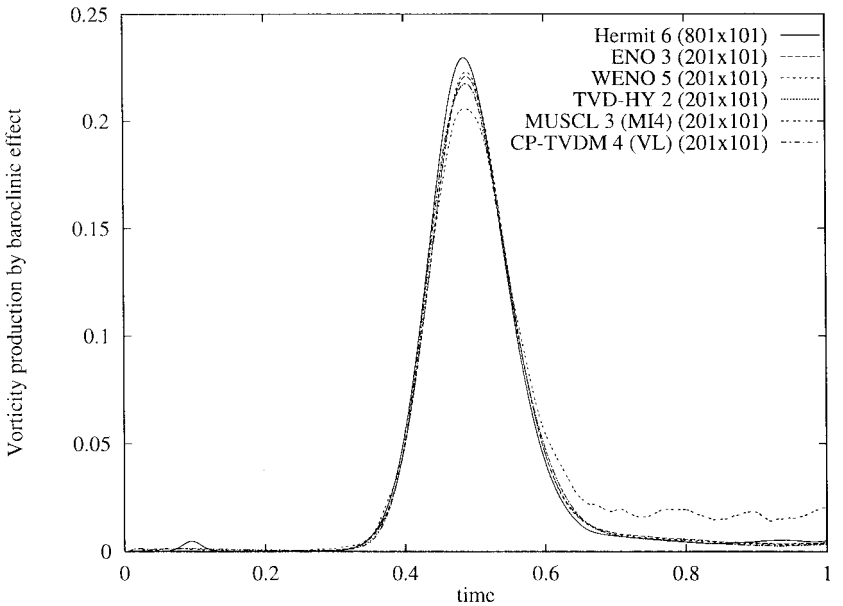

Figure 7. Time history of the integral over the computational domain of the baroclinic torque obtained by different schemes on the fine grid (201×101).

vorticity keeps a residual value at the final time of the computation (Figure 7). The vorticity is concentrated in two counterrotating vortices and no vorticity is present within the shock (Figure 10(left)).

To study the ability of each shock-capturing scheme considered herein to correctly predict the vorticity production mechanism, comparisons on the maximum of vorticity in the domain at $t = 1$ (Table III) are performed. The maximum of vorticity is located in the center of one of the counterrotating vortices. The relative errors are calculated by using the Hermit-6 scheme as reference. The TVD schemes (TVD-HY and CP-TVDM) underestimate the maximum of vorticity (3), owing to large numerical dissipation. Both TVD schemes exhibit significant errors on the maximum of ω on the coarse grid, while the results are improved on the fine grid since the errors are less than 4 per cent. MUSCL-3 and ENO-3 exhibit similar behaviors. Surprisingly good agreements with the Hermit-6 results are obtained on the fine grid while important discrepancies occur on the coarse grid. The highest order ENO schemes (MENO and WENO) give good results. They are less sensitive to the grid refinement than TVD schemes since the errors are of the same of order of magnitude on both grids. However, the overestimation of the vorticity maximum may be explained by a slight antidiffusive behavior.

Comparisons are also performed on the time evolution of the integral quantities (39) and (40). To perform accurate comparisons, zooms are provided in Figures 11 and 12. All the schemes produce vorticity at the beginning of the calculation (Figure 11(left)) since the initial shock solution, prescribed by using the Rankine–Hugoniot relations (over one grid point),

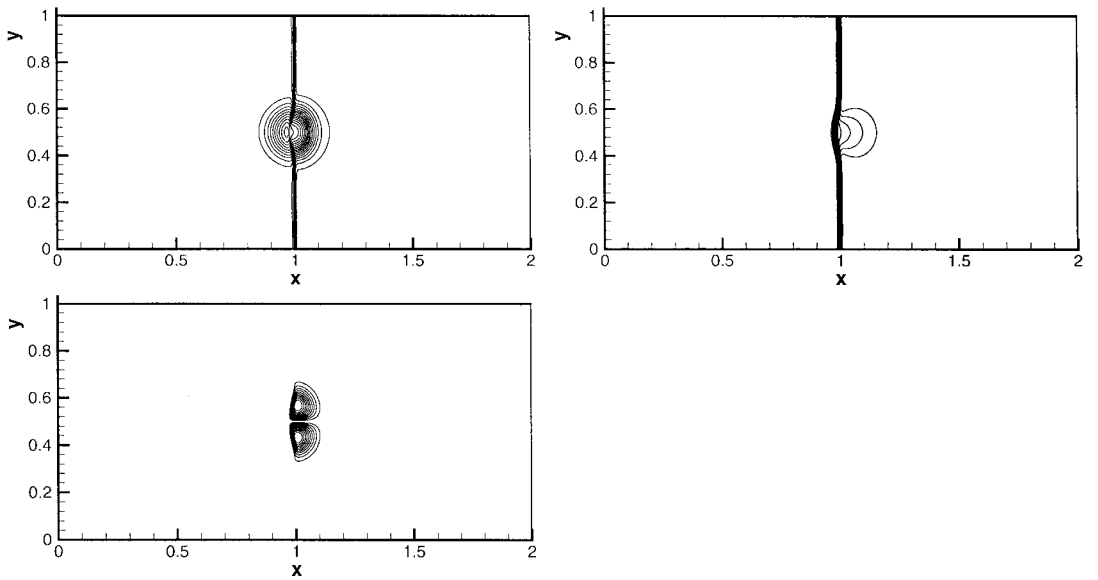

Figure 8. Interaction of a weak shock with a spot of temperature at $t = 0.5$: isocontours of the density (upper-left, 21 contours from 0.6 to 1.29), the pressure (upper right, 21 contours from 0.53 to 0.75) and the vorticity (lower-left, 20 contours from -1 to $+1$).

does not satisfy the Navier–Stokes equations. However, the more diffusive the scheme the greater the vorticity produced (Figure 11(left)). MUSCL-3 with $\beta = 4$ exhibits an anomalous behavior since the interaction starts earlier than for the other schemes (Figure 11(left)) and a large amount of vorticity is still being produced after the end of the interaction (Figure 6). This vorticity is produced by small spurious oscillations occurring just behind the shock. This must

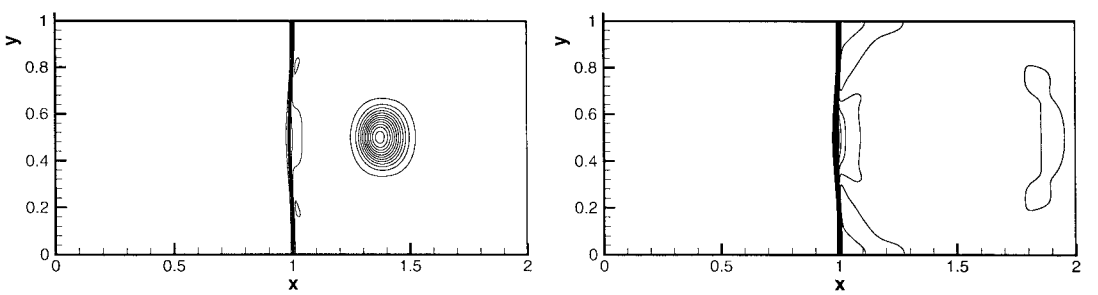

Figure 9. Interaction of a weak shock with a spot of temperature at $t = 1.0$: isocontours of the density (left, 21 contours from 0.6 to 1.29), the pressure (upper-right, 21 contours from 0.53 to 0.75).

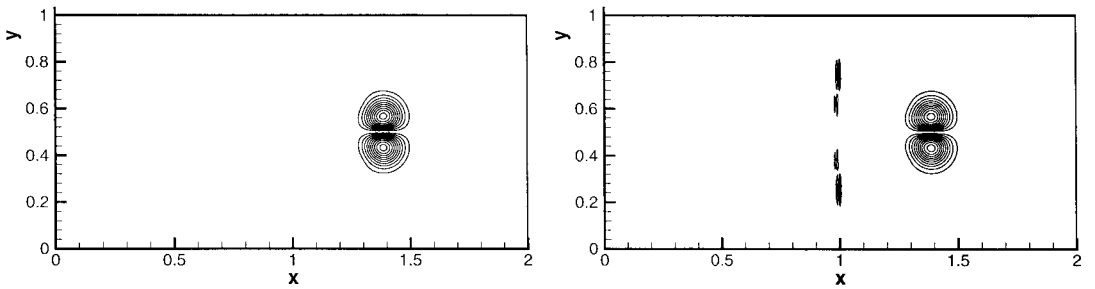

Figure 10. Interaction of a weak shock with a spot temperature at $t = 1.0$: isocontours of the vorticity (20 contours from -1 to $+1$), obtained both from the Hermit-6 schemes (left) and the WENO scheme (right).

be attributed to a numerical artifact due to the compressive behavior of the Minmod ($\beta = 4$) limiter, since using $\beta = 1$ this scheme behaves like the other schemes with, however, an important numerical diffusion. All the other shock-capturing schemes (TVD and ENO schemes) overpredict the integral of the velocity (Figure 11(right)) at the end of the interaction. This overprediction is related to the generation of vorticity within the shock, which persist until the end of the computation (see for instance, for the WENO scheme, Figure 10(right)). As mentioned above, no noticeable spurious vorticity is produced at $t = 1$ by using the Hermit-6 scheme (Figure 10(left)). The overprediction of vorticity is more important by using the ENO schemes (ENO and WENO) then by using the TVD schemes (TVD-HY and CP-TVDM). This is in agreement with the production of vorticity through baroclinic effect since the ENO schemes production is greater than the one estimated by using the TVD schemes (Figure 12). These residual discrepancies may be attributed to numerical diffusion specific to each scheme; the greater the numerical diffusion the smaller the integral of the vorticity modulus.

Table III. Maximum of the vorticity provided with the different schemes in the computational domain, at $t = 1$.

Schemes	Maximum of ω	Error (%)
Hermit-6 (801×101)	1.04558	0.0
TVD-HY-2 (101×51)	0.819093	-21.66
TVD-HY-2 (201×101)	1.01143	-3.27
MUSCL-3 (101×51)	0.92405	-11.62
MUSCL-3 (201×101)	1.04571	0.01
CP-TVDM-4 (101×51)	0.809734	-22.56
CP-TVDM-4 (201×101)	1.00509	-3.87
ENO-3 (101×51)	0.98945	-5.37
ENO-3 (201×101)	1.04432	-0.12
MENO-4 (101×51)	1.02913	-1.57
MENO-4 (201×101)	1.05081	0.50
WENO-5 (101×51)	1.06334	1.70
WENO-5 (201×101)	1.05608	1.00

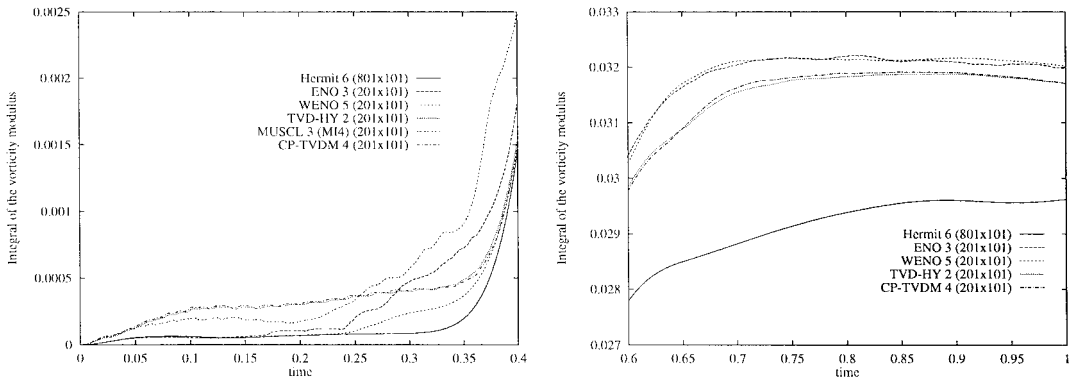

Figure 11. Zooms of the time history of the L^1_{norm} of $|\omega|$ obtained by different schemes on the fine grid (201×101).

As the initial data does not satisfy the Navier–Stokes equations, the Hermit-6 scheme yields an oscillating solution during the first time steps. The weak shock is slightly shifted upstream by a diffusion process. This explains why the maximum of production obtained by this scheme occurs a little bit earlier than for the shock-capturing schemes (Figure 12). In fact, all the

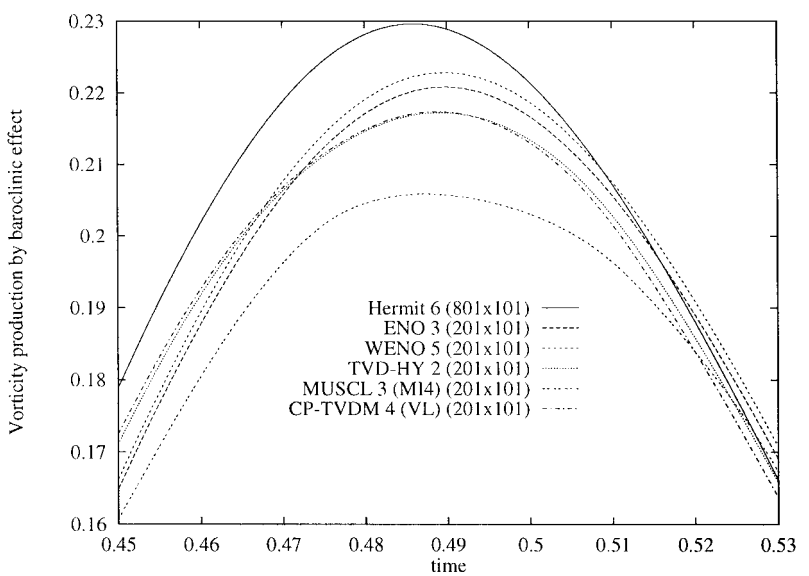

Figure 12. Zoom of the time history of the integral of the vorticity production obtained by different schemes on the fine grid (201×101).

shock-capturing schemes agree on the time of the maximum of production. Though they underestimate the production of vorticity through baroclinic effect (Figure 12). They are also sensitive to grid refinement. The best agreement with the Hermit-6 results is obtained by means of WENO-5 on the fine grid, the error on the maximum of vorticity production being of about 5 per cent (Figure 12).

Finally, the integral of the vorticity over the computational domain is calculated at each time step

$$\int_{\Omega} \omega \, \mathrm{d}\Omega$$

Since no vorticity is prescribed at the initial time this integral must be zero during the computation. The lowest values, close to computer double-precision and less than 10^{-15}, are given by WENO on the fine grid. These values are lower than those provided by Hermit-6 on the very fine grid. We underline that these values are not sensitive to grid refinement. TVD-HY-2 and ENO-3 on the coarse grid, yield the greatest values (10^{-9}), whereas on the fine grid, these values are almost one order of magnitude lower.

In conclusion, it is observed that all the shock-capturing schemes underestimate the production of vorticity by baroclinic effect. They produce an excess of vorticity within the shock even if the temperature spot is far downstream of the shock. The best results are provided by the ENO schemes (WENO-5 and MENO-4) on the fine grid with the same computational cost as the generic ENO scheme. Moreover, WENO and MENO do not exhibit great grid sensitivity on such a flow configuration.

3.3. Two-dimensional shock–vortex interaction

The last test case is tailored to investigate the capability of the shock-capturing schemes to predict the generation and the transport of acoustic waves during a shock–vortex interaction. The study is restricted to the interaction of a plane weak shock with a single isentropic vortex. The intensity of the vortex is weak enough to ensure that we deal with low shock deformations during the interaction so that the linear theory introduced by Ribner [4] can be applied.

3.3.1. Flow configuration. A squared domain $2L_0 \times 2L_0$ is considered (where L_0 is taken as the reference length scale hereafter). The dimensionless computational domain is $[0, 2] \times [0, 2]$. A stationary plane weak shock is located at $x_0 = 1$, with the same pressure jump as in the previous test case. The flow is initialized using the Rankine–Hugoniot relationships. The Reynolds number based on the velocity of the uniform flow is equal to $Re = 2000$. The same vortex as in Section 3.1 is superimposed to the base flow. The initial position of the vortex center is $x_0 = \frac{1}{2}$, $y_0 = 1$. The computations are performed with $r_c = 0.075$ and $U_c = 0.25$. As a result, the radius of the viscous core is $\frac{1}{2}$.

The boundary conditions are the same as for the interaction of the shock with the temperature spot (see Section 3.2). Two uniform grids are employed; a coarse grid with 101×101 points ($\Delta x = \Delta y = 0.01$). To obtain a reference solution, a FRS computation is performed on a very fine uniform grid (801×501) using the Hermit-6. The calculations are performed using a Courant number CFL = 0.5, corresponding to a dimensionless time step

equal to $\Delta t = 4 \times 10^{-3}$ on the coarse grid and $\Delta t = 2 \times 10^{-1}$ on the fine grid. The final dirnensionless time of the computations is 0.7.

3.3.2. Results. At the beginning of the shock–vortex interaction ($t = 0.3$) a circular acoustic wave propagating at the speed of sound is generated. This wave is clearly, seen in Figure 13, where we have plotted the static pressure obtained by WENO-5 at $t = 0.7$ on the fine mesh. Note that the vortex located just behind the shock has an elliptic shape whose main axis is parallel to the shock, in agreement with the prediction of the rapid distorsion theory.

The circumferential pressure profile along the acoustic wave is compared with the analytical prediction of Ribner [4]

$$P(\theta) = 0.0206 \sin(2\theta) - 0.0072 \cos(2\theta) - 0.0045 \sin(\theta) - 0.0023 \cos(\theta) + 0.0063 \tag{41}$$

where θ is the angle along the circular acoustic in defined in Figure 14.

For all the selected schemes, the amplitude of the pressure along the acoustic wave is about 15 times lower than that of the Ribner theory (41). This can be attributed mainly to the viscous effects, which are not taken into account in the inviscid theory of Ribner. To compare the numerical results with the analytical solution, the pressure values are shifted so that the Hermit-6 pressure value coincides with the Ribner pressure at $\theta = 0$. Moreover, the magnitudes of the corrected pressure fields, for all the numerical results, have been adjusted to fit the Ribner theory amplitude using the same rescaling. Once rescaled, the results of the Hermit-6,

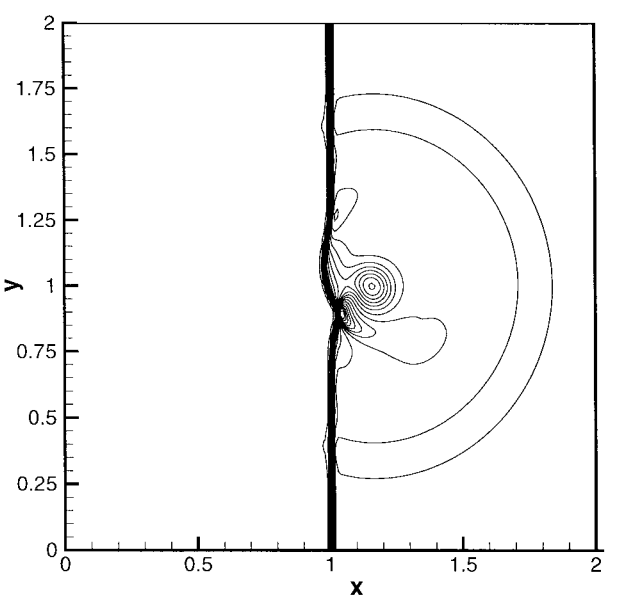

Figure 13. Two-dimensional shock–vortex interaction: isocontours of the static pressure (25 contours from 0.527 to 0.845), obtained at $t = 0.7$ using as WENO-5 scheme on the fine grid (201×201).

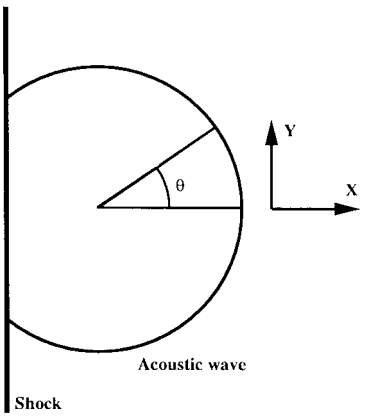

Figure 14. Sketch of the two-dimensional shock–vortex interaction: definition of the angle θ.

ENO, MENO and WENO are compared with that of the Ribner theory in Figure 15 for both grids

The results obtained by Hermit-6 on the very fine grid (801×501) are in good qualitative agreement with the Ribner theory (Figure 15), modulo a very low phase error. The location of the center of the acoustic wave (center of the vortex) and the wave radius are deduced from the Hermit-6 results at $t = 0.7$. For all the shock-capturing schemes, the circumferential

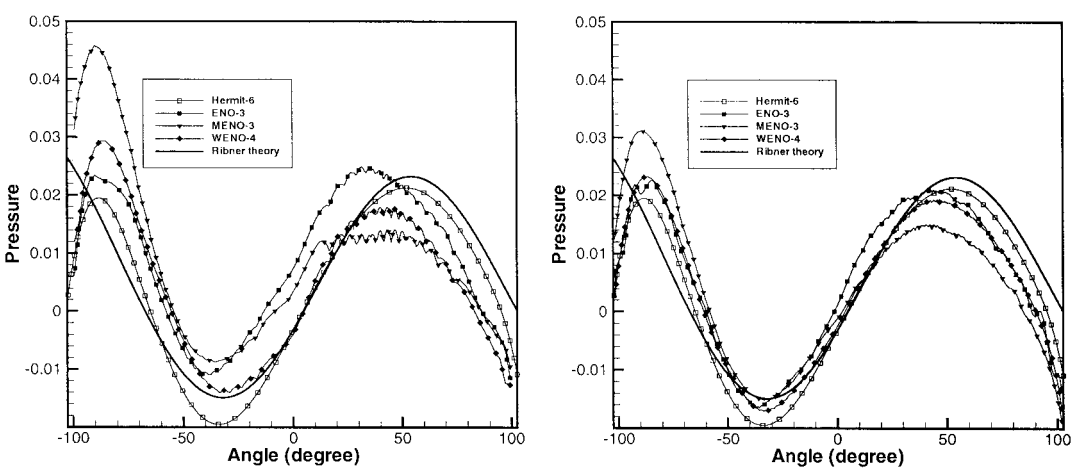

Figure 15. Comparison with the Ribner theory on the circumferential pressure profiles provided with the Hermit-6, MENO and WENO schemes on the coarse grid (101×101) (left) and the fine grid (201×201) (right).

pressure values have been calculated using these two parameters. On the fine grid, ENO-3 and WENO-5 yield results (Figure 15(right)) that are in good agreement with Hermit-6; though they exhibit a slight lagging error at positive angles. MENO-4 exhibits more discrepancies with Herrnit-6 than WENO-5. The MENO scheme underestimates the pressure at positive angles and largely overestimates the pressure at negative angles (Figure 15(right)). This may be attributed to the compressive behavior of MENO-4. ENO and MENO yield more discrepancies and lagging errors on the coarse grid (Figure 15(left)) than on the fine one. The best result is obtained by WENO-5 since it is the less sensitive to grid refinement and is on good qualitative agreement with the Ribner theory.

Since TVD and MUSCL schemes exhibit diffusive behavior, the pressure values computed by these schemes are about 3 per cent lower than those calculated by ENO schemes. To make comparisons with the Ribner theory (41), the pressure values have been corrected so that the TVD-HY pressure value coincides with the Ribner pressure at $\theta = 0$. The rescaled results, given by TVD and MUSCL schemes are compared with the Ribner theory in Figure 16. CP-TVDM and TVD schemes yield similar results, because limiter lowers by one the order of accuracy of the right-hand side of Equation (16). As a result, the compact scheme is no longer fourth-order accurate in space. Compared with the Ribner theory and the Hermit-6 results. TVD and MUSCL schemes exhibit very large discrepancies on both magnitudes and phase (Figure 16). These discrepancies increase when the grid refinement is coarser. MUSCL scheme predicts an oscillating pressure distribution along the acoustic wave (Figure 16). These oscillations are due to a numerical artifact induced by the compressive behavior of the limiter (Minmod $\beta = 4$).

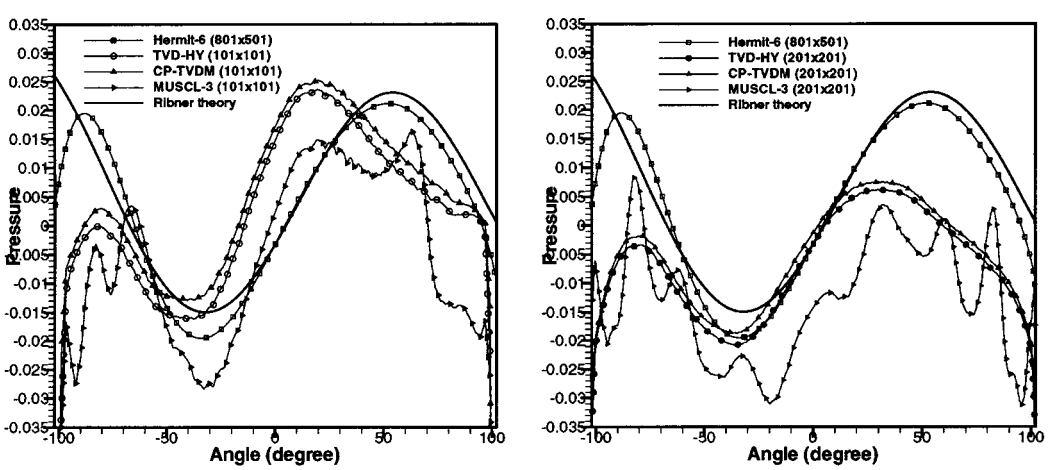

Figure 16. Comparison with the Ribner theory on the circumferential pressure profiles provided with the Hermit-6, TVD-HY, CP-TVDM and MUSCL schemes on the coarse grid (101×101) (left) and the fine grid (201×201) (right).

In conclusion, to capture and advect low amplitude phenomena, such as acoustic waves, it seems necessary to employ at least third-order accurate shock-capturing schemes without an explicit limiter. However, the role played by the limiter in such calculations is important since the MUSCL scheme exhibits a strange behavior though it is a biased third-order accurate scheme.

4. CONCLUSIONS

The assessment of the efficiency and performances of some popular shock-capturing schemes for DNS has been performed on three two-dimensional free flows at moderate Reynolds numbers. Four classes of shock-capturing schemes have been considered. TVD, MUSCL, Compact and ENO schemes. The evaluation of the diffusive and dispersive properties of each scheme has been performed by simulating the advection of a vortex in a uniform free flow. The numerical dissipation has been estimated by measuring the minimum of pressure in the vortex core and the maximum of the vertical velocity. The capability of each scheme to capture a shock and to reproduce the mechanisms of vorticity production during the interaction of the shock with inhomogeneities of the flow has been analyzed by simulating the interaction of a weak shock with a temperature spot. The efficiency of each scheme has been assessed by simulating the vorticity production by baroclinic effect during this interaction. The capability of each scheme to generate and propagate low amplitude waves such as acoustic waves has been investigated by considering the interaction of a weak shock with a vortex. The pressure profiles along the acoustic wave have been compared to that predicted by the Ribner theory.

For the three test cases considered, the results obtained by using the shock-capturing schemes have been compared to data obtained by FRS computations based on a sixth-order accurate Hermitian scheme.

The second-order Upwind-TVD scheme using the Van-Leer Harmonic limiter exhibits an overall large numerical diffusion. Due to the limiter effect this scheme is sensitive to grid refinement. The results of the Compact TVDM scheme are disappointing since they do not improve those of the second-order accurate TVD scheme. This is due to the limiter function which, in some regions of the flow, reduces by one the order of accuracy of the discrete Euler fluxes in the right-hand side of (16). As a result the CP-TVDM scheme is no longer fourth-order accurate in space.

MUSCL-3, using a Minmod limiter function with a coefficient $\beta = 4$, yields anomalous results when the flow involves shock waves; in particular, it produces low frequency oscillations just downstream of the shocks. MUSCL-3 overpredicts the production of vorticity and affects the propagation of acoustic waves. This numerical artifact is attributed to the compressive behavior of Minmod ($\beta = 4$) limiter. However, equipped with the Minmod limiter ($\beta = 4$), MUSCL-3 gives results comparable with ENO-3 in shock-free cases.

All the ENO schemes give results in closer agreement with FRS data than the TVD and CP-TVDM ones. The generic ENO schemes exhibit a slightly diffusive behavior; though it predicts well the propagation of acoustic waves. Results are improved by using the MENO version (MENO-4) with no extra computational cost compared with ENO-3. Nevertheless, MENO-4 exhibits a slightly antidiffusive behavior, which can lead to overprediction of velocity

or underprediction of pressure. The best results were obtained by WENO-5 at a computational cost similar to that of the generic ENO scheme. Moreover, WENO-5 results are not very sensitive to grid refinement (within the range studied herein).

All the investigated ENO schemes yield accurate results for the selected relevant test cases. However, in our calculations the number of grid points to represent the wave lengths (spot diameter or vortex core radius) was large, and the capability of ENO schemes to produce satisfactory results on coarse grids still needs to be accessed, especially concerning the LES of compressible flows.

ACKNOWLEDGMENTS

This study has received financial support from the SPAé DGA and ONERA (Contracts SPAé-DGA No. 95-006 and ONERA No. 23-352). Part of the computations has been carried out on the computers (Cray C90) of IDRIS/CNRS. The authors greatly acknowledge the support of these institutions.

REFERENCES

1. Moin P, Mahesh K. Direct numerical simulation: a tool in turbulence research. *Annual Review in Fluid Mechanics* 1998; **30**: 539–578.
2. Lee S, Lele SK, Moin P. Direct numerical simulation of isotropic turbulence interacting with a weak shock wave. *Journal of Fluid Mechanics* 1993; **251**: 533–562.
3. Kovasznay LSG. Turbulence in supersonic flow. *Journal of Aerospace Science* 1953; **20**(10): 657–682.
4. Ribner HS. Cylindrical sound wave generated by shock–vortex interaction. *AIAA Journal* 1985; **23**(11): 1708–1715.
5. Shu CW, Osher S. Efficient implementation of essentially non-oscillatory shock-capturing schemes. *Journal of Computational Physics* 1988; **77**: 439–471.
6. Roe PL. Approximate Riemann solvers, parameter vectors and difference schemes. *Journal of Computational Physics* 1981; **43**: 357–372.
7. Harten A. High resolution schemes for hyperbolic conservation laws. *Journal of Computational Physics* 1996; **49**: 357–393.
8. Yee HC, Harten A. Implicit TVD schemes for hyperbolic conservation laws in curvelinear coordinate. *AIAA Journal* 1987; **25**(2): 266–274.
9. Picone JM, Boris JP. Vorticity generation by shock propagation through bubbles in a gas. *Journal of Fluid Mechanics* 1988; **189**: 23–51.
10. Yee HC. Numerical experiments with s symmetric high resolution shock-capturing scheme. NASA TM-88325, 1986.
11. Yee HC. Explicit and implicit compact high resolution shock-capturing methods for multidimensional Euler equations I: formulation. NASA TM-110364, 1995.
12. Yee HC. On the implementation of a class of upwind schemes for system of hyperbolic conservation laws, NASA TM-86839, 1985.
13. Shu CW, Osher S. Efficient implementation of essentially non-oscillatory shock-capturing schemes II. *Journal of Computational Physics* 1989; **83**: 32–78.
14. Shu CW. Essentially non-oscillatory and weighted essentially non-oscillatory schemes for hyperbolic conservation laws. NASA/CR-97-206253 and ICASE Report 97-65, 1995.
15. Shu CW. Numerical experiments on the accuracy of ENO and modified ENO schemes. *Journal of Scientific Computing* 1990; **5**(2): 127.
16. Jiang GS, Shu CH. Efficient implementation of weighted ENO schemes. *Journal of Computational Physics* 1996; **126**: 202–228.
17. Sagaut P, Troff B, Garnier E, Klahr D, Comte P. Poursuite du dévelopment du code PEGASE en simulation en compressible. Rapport Technique de Synthèse ONERA RTS 20/4368 DSNA/Y, 1998.
18. Picone JM, Oran ES, Boris JP, Young TR. Theory of vorticity generation by shock wave and flame interactions. In *Dynamics of Shock Waves—Explosions and Detonations*, *94*, *Progress in Astronautics and Aeronautics*, Boven, Manson, Oppenheim, Soloukhin (eds), 1983.
19. Pernaud-Thomas B. Méthodes d'Ordre Elevé Appliquées au Calcul d'Ecoulements de Fluides Compressibles. Thèse de Doctorat de l'Université Paris VI, 1988.

